Spectrum of Engineering Sciences
ISSN (e) 3007-3138 (p) 3007-312X
Volume 4, Issue 2, 2026

THERMAL TRANSPORT IN POROUS DOMAINS FOR MHD NON-NEWTONIAN TERNARY HYBRID NANOFLUID PAST AN EXPONENTIAL STRETCHING SHEET UNDER SUCTION EFFECTS

Abdul Rehman[1], Aamir Shahzad[2], Sidra Ashraf[*3], Zeeshan Saqib[4]

[1,4]*Faculty of Sciences, Superior University Lahore, Lahore, Pakistan*
[2]*Department of Mathematics, Faculty of Natural Sciences and Technology, Baba Guru Nanak University, Nankana Sahib*
[*3]*Department of Mathematics, Faculty of Sciences, University of Sargodha, Sargodha, Pakistan*

[1]abdulkhan1122345@gmail.com, [2]aamir.shahzad@bgnu.edu.pk, [*3]sideeera@gmail.com,
[4]zeeshansaqib0314@gmail.com

DOI: https://doi.org/10.5281/zenodo.18897691

Keywords
Tri-hybrid particles, Engine oil, Exponentially, Permeable medium.

Article History
Received: 29 December 2025
Accepted: 14 February 2026
Published: 28 February 2026

Corresponding Author: *
Sidra Ashraf

Abstract
The dynamics of nanoparticle-laden flows play a crucial role in solar energy devices, thermal systems, and energy conversion applications. Motivated by these technological prospects, the present work examines the heat transfer behavior of spherical Ti–MgO–Cu nanoparticles suspended in engine oil, represented as a ternary hybrid non-Newtonian Maxwell fluid. The fluid motion is analyzed over an exponentially stretching flexible sheet, incorporating wall suction in a porous medium and influenced by magnetohydrodynamic (MHD) forces. The governing partial differential equations are reduced to ordinary differential equations via similarity transformations and solved numerically using the ***bvp4c*** *solver. The outcomes indicate that the fluid velocity rises with the exponential stretching rate, Maxwell fluid parameter, and suction intensity, while it diminishes under increasing magnetic and porous medium effects. In contrast, the temperature distribution intensifies with stronger magnetic and porous influences, whereas suction suppresses thermal levels. These results underscore the promise of ternary hybrid nanofluids for improved thermal performance in advanced engineering systems.*

1. INTRODUCTION

A ternary hybrid nanofluid represents an advanced type of nanofluid created by dispersing three distinct nanoparticle species within a base fluid, which can include water, ethylene glycol, kerosene, or even biological fluids like blood. These nanoparticles may consist of metals, metal oxides, or carbon-based structures such as graphene, each selected to improve specific thermophysical and electrochemical properties. The combined action of the three nanoparticles boosts thermal conductivity, heat transfer performance, and overall fluid stability, surpassing the capabilities of conventional or binary nanofluids. Ternary hybrid nanofluids are attracting growing attention for use in high-efficiency cooling systems, renewable energy devices, and various industrial operations, offering enhanced performance and lower energy demands. Nonetheless, issues such as particle stability, fluid compatibility, and economic feasibility must be overcome to fully exploit their practical potential.

Recent years have seen a growing interest in ternary hybrid nanofluids (THNFs) due to their potential to significantly enhance thermal performance over mono- and binary systems. Momin and Nwaokocha [1] demonstrated improved thermophysical properties in water-based ternary composite nanofluids combining MgO, ZnO, and MWCNTs, showing enhanced thermal conductivity and electrical conductivity with temperature rise. Khashi'ie *et al.* [2] investigated the Blasius flow and heat transfer characteristics of a $Cu–Al_2O_3–TiO_2$/water ternary hybrid nanofluid over a moving plate, highlighting dual solutions and notable heat transfer increases relative to binary counterparts. Sarwar *et al.* [3] proposed theoretical models for ternary nanoparticles enhancing heat transfer in MHD non-Newtonian fluid flows, emphasizing the combined influence of distinct particle types on energy transport. Ahmed *et al.* [4] conducted experimental assessments of $Al_2O_3–TiO_2–ZnO$/DW ternary composite nanofluids, reporting substantial increases in heat transfer coefficients and Nusselt numbers at elevated Reynolds numbers and nanoparticle loadings. Computational analyses have further expanded the field's scope: Sadiya and Sucharitha [5] examined MHD ternary hybrid nanofluid flow with thermochemical reactions in porous media over rotating stretching sheets, observing enhanced heat and mass transfer profiles. Theoretical investigations by authors [6-8] in Heliyon detailed magnetohydrodynamic ternary hybrid nanoliquid flows over complex geometries, reinforcing that THNFs outperform conventional single nanofluids in energy transport tasks. Experimentally, RSC Advances outlined the thermal conductivity behavior of graphene–CNT–Ag nanoparticle ternary hybrid nanofluids, elucidating how nanoparticle synergy influences transport enhancements and empirical correlation development. Tri-hybrid nanofluid studies have also explored stability and predictive modelling, where machine learning and advanced predictive techniques were used to evaluate thermo-hydraulic properties across compositions and conditions. Shinwari *et al.* [9] analyzed water-based ternary hybrid nanomaterials on stretchable curved surfaces, reinforcing their suitability for electronic cooling and heat exchange applications. Thermal Science research on micropolar MHD ternary hybrid nanofluid flows with activation energy has revealed nuanced dynamics of velocity, temperature, and concentration fields, underscoring the importance of thermophysical interactions in applied heat transfer scenarios in [10]. Additionally, Scientific Reports presented heat transfer analysis of Maxwell tri-hybridized nanofluid through a Riga wedge, showing that ternary compositions can elevate thermal conductivity in boundary layer problems compared to simpler fluid models. A recent comparative study using RSM-based [11] optimization techniques examined heat transfer of nano, hybrid, and ternary nanofluids under Cattaneo–Christov heat flux in porous media, emphasizing the distinct behaviors imparted by multi-component nanoparticle systems. Collectively, these works illustrate how ternary and tri-hybrid nanofluid systems [12] can achieve superior thermal transport, optimized flow dynamics, and enhanced heat transfer efficiency in both experimental and numerical contexts, marking them as promising candidates for advanced energy systems, heat exchangers, and industrial thermal management.

1.1. The primary target of the recently proposed framework

The present study aims to analyze the thermal performance of Ti–MgO–Cu nanomaterials dispersed in engine oil under the influence of magnetohydrodynamic (MHD) Maxwell fluid flow. The investigation considers the effects of inclined stretching sheets with porous suction and employs a ternary hybrid non-Newtonian Maxwell fluid model to explore how spherical nanoparticles impact the heat transfer characteristics of the base fluid. Key control parameters examined include mass flux, porosity, electromagnetic field strength, relaxation time, time- dependent relaxation coefficient, and convection effects. The results of this analysis provide insights into the role of these parameters in enhancing the thermal efficiency of engine oil embedded with hybrid nanoparticles.

2. Underlying Mathematical Theory

A steady, two-dimensional laminar flow past a stretching sheet with suction within a porous medium is analyzed for an electro-viscous Maxwell ternary hybrid nanofluid, subjected to a constant transverse magnetic field. The governing equations describing this flow problem are presented as follows

$$\frac{\partial u}{\partial x}+\frac{\partial v}{\partial y}=0, \tag{1}$$

$$\left(u\frac{\partial u}{\partial x}+v\frac{\partial u}{\partial y}\right)=\frac{\mu_{thnf}}{\rho_{thnf}}\frac{\partial^2 u}{\partial y^2}-\frac{\beta}{\rho_{thnf}}\left(u^2\frac{\partial^2 u}{\partial x^2}+v^2\frac{\partial^2 u}{\partial y^2}+2uv\frac{\partial^2 u}{\partial x\partial y}\right)-\frac{g(\rho\beta_T)_{thnf}}{\rho_{thnf}}(T-T_\infty)+\frac{\sigma_{thnf}}{\rho_{thnf}}B_0^2u-\frac{\nu_{thnf}}{K_o}u\,, \tag{2}$$

$$\left(\rho C_p\right)_{thnf}\left(u\frac{\partial T}{\partial x}+v\frac{\partial T}{\partial y}\right)=k_{thnf}\frac{\partial^2 T}{\partial y^2}. \tag{3}$$

Here (1-3) expressions are suspended with boundary constraints as follows;

$$\left.\begin{aligned} u(x,0)=U_w(x)=U_0e^{x/L}\ ,v=-v_o\,,T(x,0)=T_w\,,C(x,0)=C_w \quad at\ \ y=0,\\ u\to 0,T\to T_\infty,C\to C_\infty. \end{aligned}\right\} \tag{4}$$

In this context, x and y represent the velocity components, while T, T_W, T_∞, C, C_W, and C_∞ denote the bulk temperature, wall (or surface) temperature, surrounding fluid temperature, solute concentration, surface concentration, and ambient concentration, respectively.

3. Numerical Solution Strategy

In this section, the complete methodology of solution is presented, detailing how expressions (1– 3) under the fluid flow conditions in (4) are addressed. The following subsections outline the procedure by which the PDEs (1–3) with conditions (4) are transformed into ODEs. Additionally, the approach employed to solve the resulting ODEs is described.

3.1 Change-of-variables method

In this part, the similarity transformation discussed in (5) will be helpful to reduce the coupled system and nonlinear PDEs described in (1–3), under the flow conditions given in (4), into a set of ODEs. The corresponding of variables are introduced given below:

$$\begin{gathered} u=U_0e^{x/L}\,f'(\eta),v=-\sqrt{\frac{vU_0}{2L}}e^{x/2L}[\,f(\eta)+\eta f'(\eta)] \\ \psi=\sqrt{2vLU_0}e^{x/2L}f(\eta),\qquad \theta(\eta)=\frac{T-T_\infty}{T_o-T_\infty},\eta=\sqrt{\frac{U_0}{2vL}}ye^{x/2L} \end{gathered} \tag{5}$$

By introducing the similarity variables from (5) into (1–4) renders (1) identically satisfied, with the residual expressed as follows;

$$\frac{\frac{\mu_{thnf}}{\mu_f}}{\frac{\rho_{thnf}}{\rho_f}}f''' - 2f'^2 - ff'' - \frac{\lambda_1}{\frac{\rho_{thnf}}{\rho_f}}(f^2f''' - 2ff'f'') - \frac{\frac{(\rho\beta_T)_{thnf}}{(\rho\beta_T)_f}}{\frac{\rho_{thnf}}{\rho_f}}\lambda\theta - \frac{\frac{\sigma_{thnf}}{\sigma_f}}{\frac{\rho_{thnf}}{\rho_f}}Mf' - \frac{\mu_{thnf}}{\mu_f}Kf' = 0, \tag{6}$$

$$\frac{\frac{k_{thnf}}{k_f}}{\frac{(\rho C_P)_{thnf}}{(\rho C_P)_f}}\frac{1}{Pr}\theta'' + (f\theta' - f'\theta) = 0 \tag{7}$$

Considered boundary constraints

$$\left.\begin{array}{l} f = S,\ f' = 1,\ \theta = 1,\ \text{at}\,\eta = 0 \\ f' \to 0,\ \theta \to 0,\ \text{as}\,\eta \to \infty \end{array}\right\}, \tag{8}$$

Where, $\lambda_1 = \frac{\beta U_0}{\rho_f L}$ is viscoelastic relaxation parameter, with β as relaxation parameter of time, $\lambda = \frac{g(\beta_T)_f \Delta T}{c^2 x}$ is thermal buoyancy coefficient with $\Delta T = (T_w - T_\infty)$, $M = \frac{\sigma_f B_{0L}^2}{U_0 \rho_f}$ is Lorentz number, $K = \frac{v_f L}{K_o U_0}$ is dimensionless porosity parameter, $Pr = \frac{v_f}{\alpha_f}$ is thermal boundary layer number with $\alpha = \frac{\kappa_f}{(\rho c_P)_f}$ as heat penetration rate, $S = \frac{v_o}{\sqrt{U_0 v_{f/2L}}}$ is negative flux parameter $(v_o > 0)$. Here, η be known as variable of similarity.

3.2. Principal engineering parameters

The fundamental key parameters under consideration include the skin friction coefficient and Nusselt number, expressed as

$$C_f = \frac{\mu_{thnf}}{\rho_{thnf}}\sqrt{1/2vLU_0 e^{x/L}}f''(0), \mathrm{Nu}_x = x\sqrt{\frac{U_0}{2vL}}ye^{x/2L}(-\theta'(0)) \tag{9}$$

Using equation (5), in (9), and doing basic algebraic steps, we have

$$Re_x^{1/2}C_f = \sqrt{\frac{\mu_{thnf}}{2\rho_{thnf}v_{thnf}}}f''(0), Re_x^{-1/2}Nu_x = -\frac{x}{2L}\theta'(0) \tag{10}$$

Table 1: Thermal-physical attributes

Properties	$\rho(Kg/m)$	C_p ($JKg^{-1}K^{-1}$)	k ($Wm^{-1}K^{-1}$)	$\beta \times 10^{-5}K^{-1}$
Base fluid (Engine Oil)	884.0	1910.0	0.144	70.0
$Ti\ (s_1)$	4510	540	20.9	0.9

MgO (s_2)	3560.0	955.0	45.0	1.26
Cu (s_3)	8933	385.0	400.0	5.1

3.3. Computational Strategy

The expressions (7-8) with boundary constraints shown in (9) are estimated by applying built-in numerical solver bvp4c. Then equations (7-8) with B. Cds discussed in (9) are firstly converted into ODEs system of primary order and then replace into said technique for numerical fallout. The procedure is given below:

$$\zeta(1) = f, \zeta(2) = f', \zeta(3) = f'', \zeta(4) = \theta, \zeta(5) = \theta' \qquad (11)$$

$$\zeta\zeta 1 = \frac{-\left(2\zeta(2)^2 - \zeta(1)\zeta(3) + \frac{\lambda_1}{\frac{\rho_{hnf}}{\rho_f}}\left[\zeta(2)^2\zeta(3) + 2\zeta(2)\left(\zeta(1) + \eta\zeta(2)\right)\zeta(3)\right] - \frac{\frac{(\rho\beta_T)_{hnf}}{(\rho\beta_T)_f}}{\frac{\rho_{hnf}}{\rho_f}}\lambda\theta - \frac{\frac{\sigma_{hnf}}{\sigma_f}}{\frac{\rho_{hnf}}{\rho_f}}M\zeta(2) + \frac{\mu_{hnf}}{\mu_f}K\zeta(2)\right)}{\left(\frac{\frac{\mu_{hnf}}{\mu_f}}{\frac{\rho_{hnf}}{\rho_f}} - \frac{\lambda_1}{\frac{\rho_{hnf}}{\rho_f}}\left(\zeta(1) + \eta\zeta(2)\right)^2\right)} \qquad (12)$$

$$\zeta\zeta 2 = -\frac{Pr(f\theta' - \theta f')}{\frac{\frac{k_{hnf}}{k_f}}{\frac{(\rho C_P)_{hnf}}{(\rho C_P)_f}}} \qquad (13)$$

Boundary conditions

$$\left.\begin{array}{l}\zeta(1) = S,\ \zeta(2) = 1,\ \zeta(4) = 1,\ \text{at}\ \eta = 0 \\ \zeta(2) \to 0,\ \zeta(4) \to 0,\ \text{as}\ \eta \to \infty\end{array}\right\}. \qquad (14)$$

4. Results and Discussion

Here, the conclusion of the discussed technique produced by main numerical solver technique are shown in tabular and visualized representation. Results for f' and θ are graphed, where f' and θ are known as velocity and temperature representations, the wall drags coefficient $Re^{1/2}C_f$ convective heat transfer coefficient ratio $Re^{-1/2}\ Nu$ are visualized with tables as well. The analyzed outcomes are computed with respect to several parameters: Maxwell fluid parameter λ_1, Lorentz force parameter M, buoyancy affected number λ, thermal boundary layer parameter Pr, dimensionless porosity K, and aspiration parameter S ($S > 0$).

Figs. 1-2 are visualized the rise or downfall in velocity component f' and temperature component θ under according to the observation of magnetic number M. Basically, the visualized effects shown changing in M affected to velocity get low and temperature get high for both Ti/engine oil and $Ti - MgO$/engine oil cases. It is due to fact that increment in M, causes to produce higher impedance, thereby impeding flow and diminishing thermal rise. Noticeable point, is magnitudes of curves of velocity for Ti/engine oil are larger than $Ti - MgO$/engine oil. Furthermore, the phenomenon for θ is completely reverse. The augmentation of f' with the effects of relaxation time parameter $\lambda_1$are shown in Fig. 3. As λ_1, rise, f' is increases accordingly. Moreover, graphs for Ti/engine oil are higher than that of $Ti - MgO$/engine oil. Fig. 4, is highlighting the involvement of angle of inclination ξ on f'. The visualized effects are showing that as ξ is changed from $\xi = 0.0, \frac{\pi}{6}, \frac{\pi}{3},$ to $\pi/2$, f' is reinforced. Permeable medium K effects on f' and θ are presented in Figs. 5-6

It is viewed that as K is enhanced, f' goes to decline. Moreover, curves of f' for Ti/engine oil are more than that of $Ti - MgO$/engine oil. But, for θ reverse attitudes are found. Figs. 5-6, are generated to visualized the behavior of f' and θ physically in contrast with distinct values for parameter of suction S (S > 0), respectively. As, S raised, f' is increased and θ is decreased. It is worthy to note that for Al_2O_3/kerosene oil, the curves of f' are much stronger than that of $Ti - MgO$/engine oil. But, for the case of θ entire opposite phenomenon is seen.

In Table 2, the conclusions for permeable parameter K on wall shear coefficient $Re^{1/2}C_f$ and thermal boundary layer number $Re^{-1/2}Nu$ are visualized. It is noted that as K is enhanced the wall shear coefficient gets enhanced too but thermal boundary layer number is minimized. In Table 3, the behavior of $Re^{1/2}C_f$ and $Re^{-1/2}Nu$ under effects by number of Prandtl is addressed. As Pr is intensified $Re^{1/2}C_f$ is risen and $Re^{-1/2}$ Nu is reduced gradually.

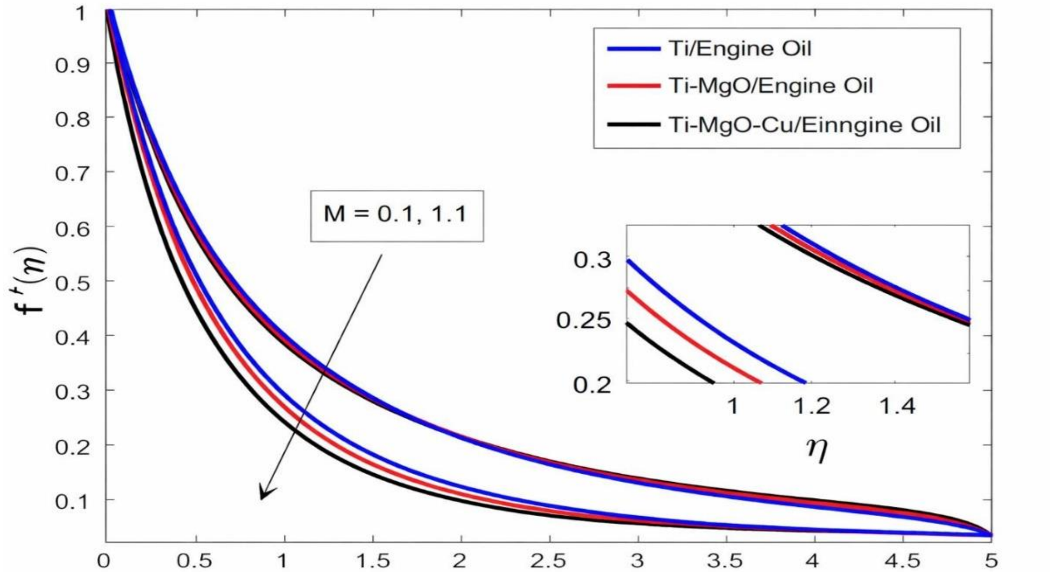

Fig. 1: Visualized Effects in f' on contrasted with M Pr=7.2, M=1.25; B = 0.15; Gr=0.15; K = 1.25; S=0.0; Ec=0.15; L1=0.15; Re=0.15; Rd=1.25;

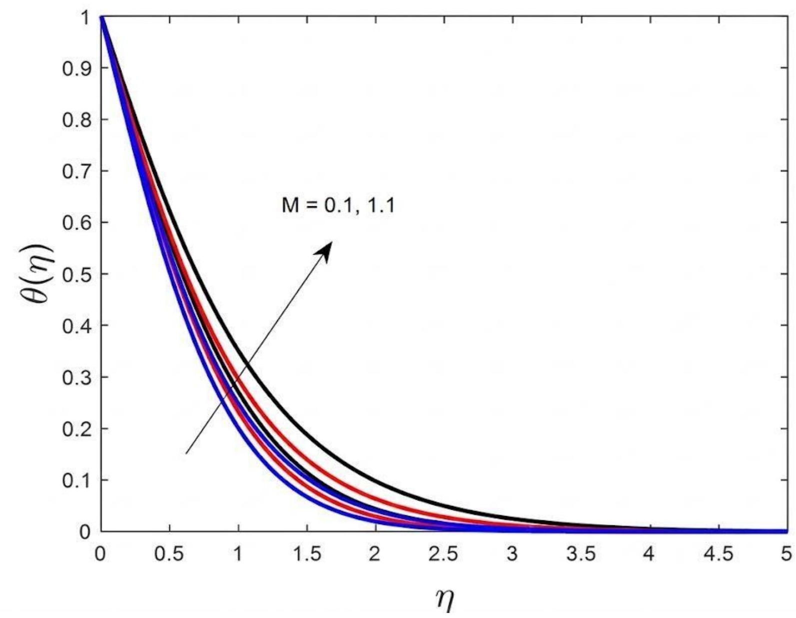

Fig. 2: Visualized Effects in $\boldsymbol{\theta}$ on contrasted with $\boldsymbol{M}$ Pr=7.2, M=1.25; B = 0.15; Gr=0.15; K = 1.25; S=0.0; Ec=0.15; L1=0.15; Re=0.15; Rd=1.25;

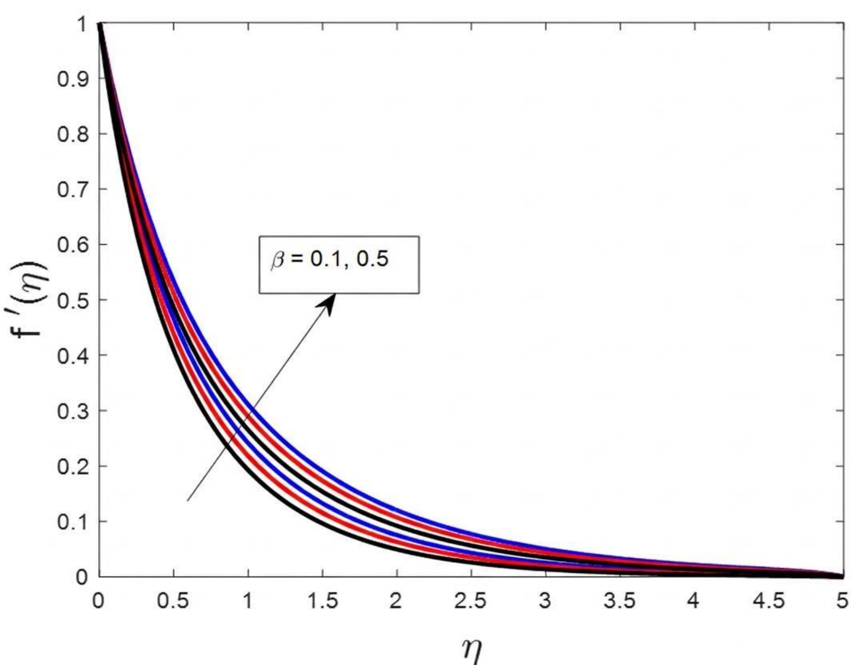

Fig. 3: Visualized Effects in $\boldsymbol{f'}$ on contrasted with $\boldsymbol{\lambda_1}$ Pr=7.2, M=1.25; B = 0.15; Gr=0.15; K = 1.25; S=0.0; Ec=0.15; L1=0.15; Re=0.15; Rd=1.25;

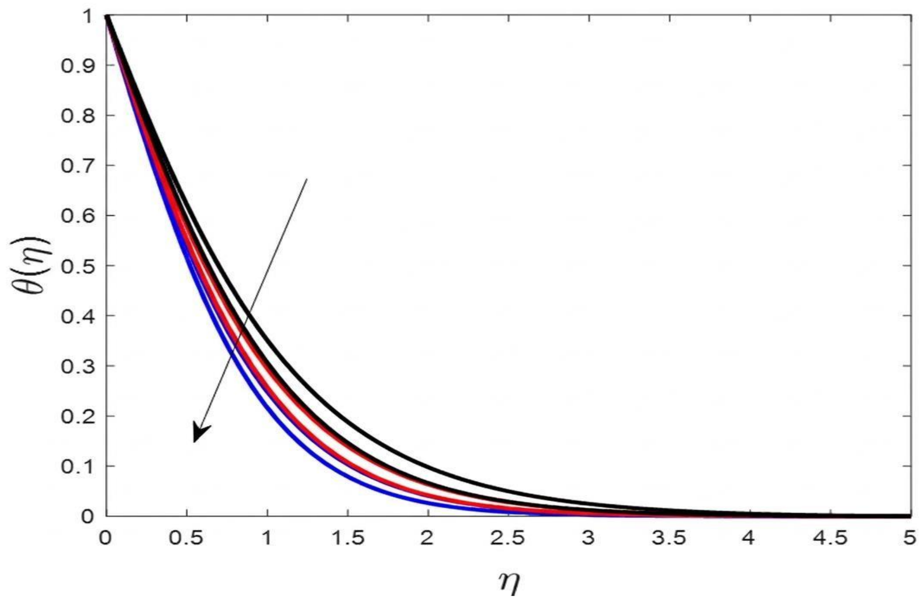

Fig. 4: Visualized Effects in f' on contrasted with ξ Pr=7.2, M=1.25; B = 0.15; Gr=0.15; K = 1.25; S=0.0; Ec=0.15; L1=0.15; Re=0.15; Rd=1.25;

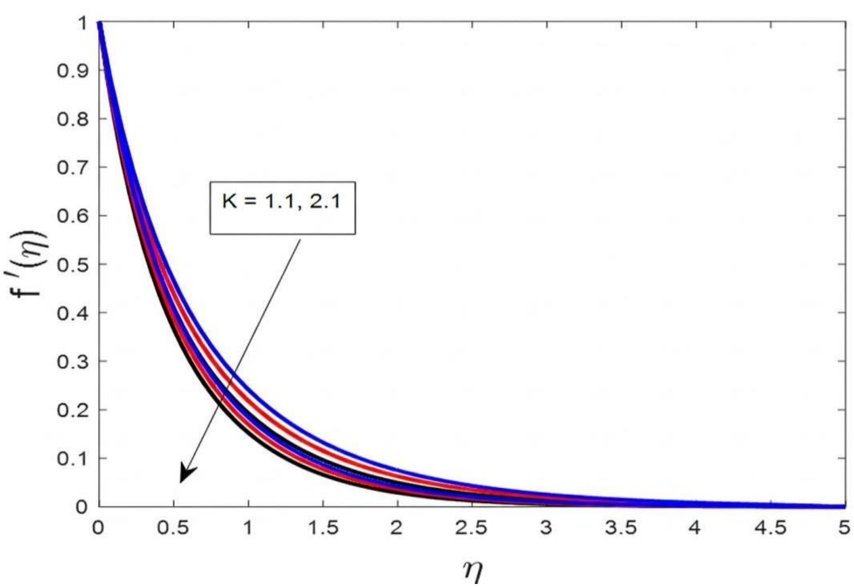

Fig. 5: Visualized Effects in f' on contrasted with K Pr=7.2, M=1.25; B = 0.15; Gr=0.15; K = 1.25; S=0.0; Ec=0.15; L1=0.15; Re=0.15; Rd=1.25;

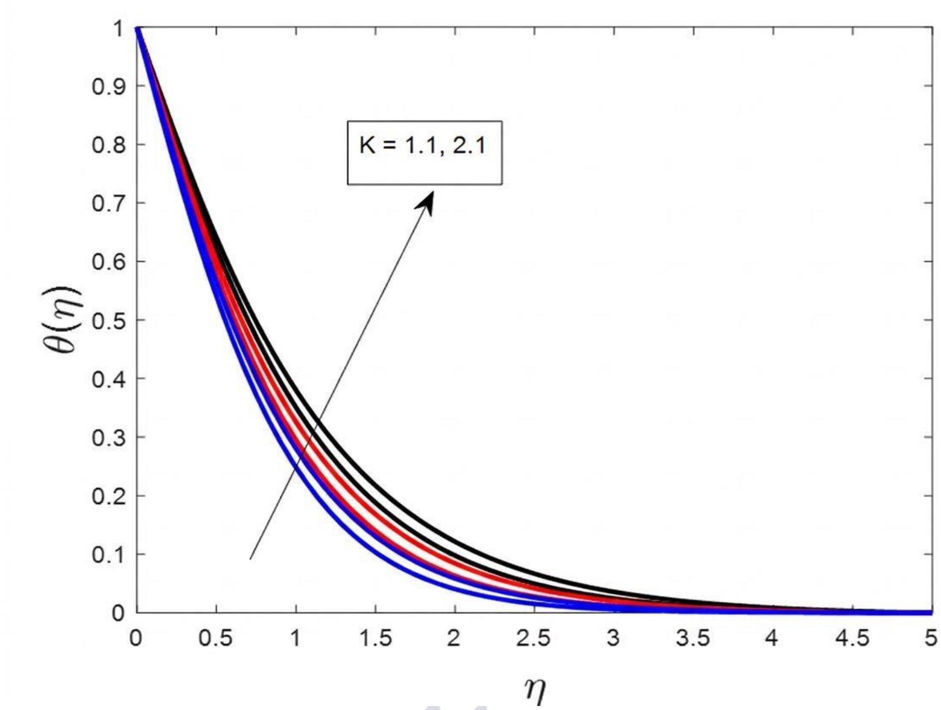

Fig. 6: Visualized Effects in θ on contrasted with K Pr=7.2, M=1.25; B = 0.15; Gr=0.15; K = 1.25; S=0.0; Ec=0.15; L1=0.15; Re=0.15; Rd=1.25;

Table 2: Numerical Values of $a)\ Re^{1/2}C_f b)\ Re^{-1/2}Nu\ for\ M = 1.6, Pr = 7.0,, \phi_1 = \phi_2 = 0.01, \lambda_1 = 0.1, \lambda = 0.1, \xi = \frac{\pi}{6}, S = 0.2$ against several values of Pr

K	$Re^{1/2}C_f$	$Re^{-1/2}Nu$
1.125	-1.454	2.6895
2.125	-1.7302	2.6424
3.125	-1.9743	2.6017
4.125	-2.1932	2.5655

Table 3: Numerical Values of $a)\ Re^{1/2}C_f b)\ Re^{-1/2}Nu\ for\ M = 0.75, K = 1.1, \phi_1 = \phi_2 = 0.01, \lambda_1 = 0.1, \lambda = 0.1, \xi = \frac{\pi}{6}, S = 0.2$ against several values of Pr

Pr	$Re^{1/2}C_f$	$Re^{-1/2}Nu$
1.01	2.085	3.01
5.01	2.085	4.209
7.01	2.085	4.541
10.01	2.085	4.939

Conclusion

In this study, the influence of suction and magnetohydrodynamic effects on three- particle nanofluid flow and transportation of heat, modeled through a Non-newtonian electrically conducting fluid over an exponential stretching sheet in a permeable medium, has been analyzed. The principal findings are summarized as follows:

- The rise in velocity of fluid with higher values of the inclination angle parameter, the Maxwell relaxation parameter, and the negative pressure parameter.
- Conversely, seen the downfall of velocity when the permeable medium resistance parameter and electromagnetic parameter increase.
- The temperature of the fluid rises with stronger magnetic effects and greater porous resistance, whereas it declines with increasing suction strength.
- An increase in the porous medium parameter enhances the wall shear coefficient while reducing the dimensionless heat transfer number.
- Similarly, increasing the Prandtl number leads to a gradual rise in skin friction and a corresponding decrease in the Nusselt number.
- All graphical profiles satisfy the prescribed boundary conditions and approach them asymptotically.

REFERENCES

[1]. Momin, M., Nawaokocha, C. N., Sharifpur, M., Cheraghian, G., Meyer, J, P., & Abd El Rahman, M. (2025). Investigation of thermal and electrical properties of ternary composite nanofluids using MgO, ZnO, and MWCNT nanoparticles. *Journal of Results in Physics*, 70(108139),

[2]. Khashi'ie, N. S., Abdollah, M. F. B., Waini, I., & Pop, I. (2025). Blasius flow of a ternary hybrid nanofluid over a moving plate. *JP Journal of Heat and Mass Transfer*, 38(3), 447- 456.

[3]. Sarwar, N., Jahangir, S., Asjad, M. I., & Eldin, S. M. (2022). Application of ternary nanoparticles in the heat transfer of an MHD non-Newtonian fluid flow. *Journal of Micromachines*, 13(12).

[4]. Adun, H., Abid, M., Kavaz, D., Hu, Y., & Hj Zaini, J. (2023). Optimizing the thermophysical behavior of a novel ternary hybrid nanofluid for energy applications through experimental research. *Journal of Heliyon*, 10(12).

[5]. Sadiya, A. B., & Sucharitha, G. (2025). Computational analysis of MHD ternary hybrid nanofluid flow with thermochemical reactions through a porous medium on a rotating stretching sheet. *Journal of Discover Nano*, 20(168).

[6]. Ramzan, M., Kumam, P., Lone, S. A., Seangwattana, T., Saeed, A., & Gala, M. A. (2023). A theoretical analysis of the ternary hybrid nanofluid flows over non-isothermal and non-isosolutal multiple geometries. *Journal of Heliyon*, 9(4).

[7]. Trinh, P. V., Anh, N. N., Phuong, M. T., Nguyen, V. T., Hau, T. V., Tuan, D., Huyen, N. T., Thanh, C. T., Hao, N. V., Phommahaxay, M., Mai, N. T. N., Hong, P. N., Minh, P. N., Thang, B. H. & Chuc, N. V. (2026). Experimental study on the thermal conductivity of graphene–carbon nanotube–silver nanoparticle ternary hybrid nanofluids. *Journal of Royal Society of Chemistry*, 16(4).

[8]. Adogbeji, V. O., Atofarati, E. O., Govinder, K., Sharifpur, M., & Meyer, J. P. (2025). Tri-hybrid nanofluids for thermal applications: stability, magneto-hydrodynamics, and machine learning prediction. *Journal of Multiscale and Multidisciplinary Modeling, Experiments and Design*, 8(411).

[9]. Shinwari, W., Hayat, T., Abbas, Z., & Momani, S. (2023). A numerical study on the flow of water-based ternary hybrid nanomaterials on a stretchable curved sheet. *Journal of Nanoscale Advances*, 22(5), 6249-6261.

[10]. Mahariq, I., Islam, S., Abas, S. A., Ali, I., Fiza, M., Hakeem ullah & Akgul, A. (2025). Thermal dynamics of ternary hybrid micropolar magnetohydrodynamics nanofluid-flow with activation energy over a heated curved surface. *Journal of Thermal Dynamics of Ternary Hybrid Micropolar Thermal Sciences*, 29(4B), 3149-3165.

[11]. Zulqarnain, R. M., Nadeem, M., Siddique, I., Ahmed, H., Asker, S. & Samar, M. (2023). Heat transfer analysis of Maxwell tri-hybridized nanofluid through Riga wedge with fuzzy volume fraction. *Scientific Reports*, 13(18238).

[12]. Afzal, U., Masood, K., Zafar, A. A., Farade, R. A., Shah, N. A. & Chung, J. D. (2026). Comparative RSM-based study of nano, hybrid, and ternary nanofluid heat transfer with Cattaneo–Christov flux in porous media. *Journal of Nano Technology Reviews.*

[13]. Gireesha, B. J. & Anitah, L. (2024). Impact of Shape Dependent Ternary Hybrid Nanoliquid Flow through a Microchannel with Quadratic Thermal Radiation: Irreversibility Analysis. *Journal of Applied and Computational Mechanics,* 10(4), 729-741.